Zhang et al. *NPG Asia Materials* (2022)14:22
https://doi.org/10.1038/s41427-022-00369-5

NPG Asia Materials

ARTICLE Open Access

# Toward tunable quantum transport and novel magnetic states in $Eu_{1-x}Sr_xMn_{1-z}Sb_2$ ($z < 0.05$)

Qiang Zhang[1,2], Jinyu Liu[3], Huibo Cao[1], Adam Phelan[2], David Graf[4], J. F. DiTusa[2], D. Alan Tennant[1,5,6] and Zhiqiang Mao[3,7]

**Abstract**

Magnetic semimetals are very promising for potential applications in novel spintronic devices. Nevertheless, realizing tunable topological states with magnetism in a controllable way is challenging. Here, we report novel magnetic states and the tunability of topological semimetallic states through the control of Eu spin reorientation in $Eu_{1-x}Sr_xMn_{1-z}Sb_2$. Increasing the Sr concentration in this system induces a surprising reorientation of noncollinear Eu spins to the Mn moment direction and topological semimetallic behavior. The Eu spin reorientations to distinct collinear antiferromagnetic orders are also driven by the temperature/magnetic field and are coupled to the transport properties of the relativistic fermions generated by the 2D Sb layers. These results suggest that nonmagnetic element doping at the rare earth element site may be an effective strategy for generating topological electronic states and new magnetic states in layered compounds involving spatially separated rare earth and transition metal layers.

## Introduction

Dirac/Weyl semimetals have attracted intense research interest due to their exotic quantum phenomena, as well as their promise for applications in next generation, more energy-efficient electronic devices[1–3]. Magnetic Dirac/Weyl semimetals are especially attractive since the coupling of Dirac/Weyl fermions to the additional spin degree of freedom may open up a new avenue for tuning and controlling the resulting quantum transport properties[4–6]. To date, several magnetic semimetals have been reported, and most of them were discovered in stoichiometric compounds, such as $SrMnBi_2$[7], $Mn_3Sn$[8], RAlGe(R = rare earth)[9], $Co_3Sn_2S_2$[10,11], and $Co_2MnGa$[12,13]. Finding a strategy to control a topological state by tuning magnetism is highly desirable and requires a clear understanding of the interplay between the magnetism and the topological electronic state. This goal can be achieved by investigating the coupling between the structure and magnetic and electronic phase diagrams in tunable magnetic topological materials.

The large family of ternary $AMnCh_2$ "112" compounds (A = alkali earth/rare earth elements, Ch = Bi or Sb)[6,7,14–16] are particularly interesting since a few of them have been reported to be magnetic Dirac semimetals where the Bi or Sb layers host relativistic fermions. $AMnCh_2$ (A = Ce, Pr, Nd, Eu, Sm; C = Bi or Sb)[14,16–18] possesses two magnetic sublattices, formed by the magnetic moments of rare earth A and Mn, respectively, in contrast with other compounds, which have only Mn magnetic lattice in this family. The conducting Bi/Sb layers and the insulating magnetic Mn–Bi(Sb) and Eu layers are spatially separated, which makes them good candidates for exploring the possible interplay between Dirac fermions and magnetism. For $EuMnBi_2$, both the Eu and Mn moments point in the out-of-plane direction and generate two AFM lattices in the ground state[16]. Previous studies have also shown that when the Eu AFM order undergoes a spin-flop transition in a moderate field range, interlayer conduction is strongly suppressed, thus resulting in a stacked quantum Hall effect. Interestingly, $EuMnSb_2$ exhibits distinct

Correspondence: Qiang Zhang (zhangq6@ornl.gov)
[1]Neutron Scattering Division, Oak Ridge National Laboratory, Oak Ridge, TN 37831, USA
[2]Department of Physics and Astronomy, Louisiana State University, Baton Rouge, LA 70803, USA
Full list of author information is available at the end of the article
These authors contributed equally: Qiang Zhang, Jinyu Liu.

properties from $EuMnBi_2$, and conflicting results have been reported[17–19]. The magnetotransport properties reported by Yi et al.[17] are not indicative of a Dirac semimetallic state, while Soh et al.[18] observed linear band dispersion near the Fermi level in Angle-resolved photoemission spectroscopy measurements of $EuMnSb_2$ and claimed that it may be a Dirac semimetal. Moreover, the magnetic structure of $EuMnSb_2$ is thought to be distinct from that of $EuMnBi_2$, with controversial reports on Eu and Mn moments being perpendicular[18] or canted to each other[19]. It is therefore important to resolve the controversy about the magnetic and physical properties of $EuMnSb_2$ and to explore whether EuMnSb and its derivatives could host Dirac fermions. Additionally, it is known that in many-layered compounds involving spatially separated rare earth and manganese layers such as RMnAsO (R = Nd or Ce)[21,22] and RMnSbO (R = Pr or Ce)[22,23], the moment of rare earth elements ordered at low temperatures usually drives Mn spin reorientation to its moment direction. Given that there are two magnetic sublattices of Eu and Mn with an expected 4*f*–3*d* coupling between them in $EuMnSb_2$, the chemical substitution of Eu by nonmagnetic elements may achieve interesting magnetic states by tuning the magnetic interactions, which may control the transport and magnetotransport properties.

In this article, we report comprehensive studies on a tunable Dirac semimetal system $Eu_{1-x}Sr_xMn_{1-z}Sb_2$, which exhibits a variety of novel magnetic states tunable by the Eu concentration, temperature, and magnetic field. The evolution of the magnetic states of this system is found to be coupled to the quantum transport properties of Dirac fermions. Through single-crystal X-ray diffraction, neutron scattering, magnetic and high-field transport measurements, we established a rich phase diagram of the crystal structure, magnetism, and electronic properties of $Eu_{1-x}Sr_xMn_{1-z}Sb_2$. The increase in Sr concentration in $Eu_{1-x}Sr_xMn_{1-z}Sb_2$ induces not only lattice symmetry breaking and surprising Eu spin reorientation to the Mn moment direction but also topological semimetallic states for $x \geq 0.5$. Furthermore, the quantum transport properties can be tuned by the different Eu spin reorientations to collinear AFM orders induced by the temperature and external magnetic field. The in-plane and out-of-plane components of the canted Eu magnetic order are found to influence the intralayer and interlayer conductivities of Dirac fermions generated by the 2D Sb layers, respectively. These results establish a new unique material platform for exploring Dirac band tuning by magnetism.

## Materials and methods

### Crystal growth

The $Eu_{1-x}Sr_xMn_{1-z}Sb_2$ single crystals were grown using a self-flux method. The starting materials with stoichiometric mixtures of Eu/Sr, Mn, and Sb elements, i.e., $EuMnSb_2$, $Eu_{0.8}Sr_{0.2}MnSb_2$, $Eu_{0.5}Sr_{0.5}MnSb_2$, and $Eu_{0.2}Sr_{0.8}MnSb_2$, were put into small alumina crucibles and sealed in individual quartz tubes in an argon gas atmosphere. The tube was heated to 1050 °C for 2 days, followed by subsequent cooling to 650 °C at a rate of 2 °C/h. Plate-like single crystals were obtained. The compositions of all the single crystals were examined using energy-dispersive X-ray spectroscopy. The composition of the $x = 0$ parent compound was also characterized by fitting to single-crystal X-ray diffraction data.

### Single-crystal X-ray and neutron diffraction measurements and neutron data analysis

A crystal of $x = 0$ was mounted onto glass fibers using epoxy, which was then mounted onto the goniometer of a Nonius KappaCCD diffractometer equipped with Mo Kα radiation ($\lambda = 0.71073$ Å). After the data collection and subsequent data reduction, SIR97 was employed to provide a starting model, SHELXL97 was used to refine the structural model, and the data were corrected using extinction coefficients and weighting schemes during the final stages of refinement[24,25]. To investigate the crystal and magnetic structures, neutron diffraction measurements were conducted with the four circle neutron diffractometer (FCD) located in the High Flux Isotope Reactor at Oak Ridge National Laboratory. To further distinguish between tetragonal and orthorhombic structures for $x = 0$, neutrons with a monochromatic wavelength of 1.003 Å without λ/2 contamination are used via the silicon monochromator from (bent Si-331)[26]. For other $Eu_{1-x}Sr_xMn_{1-z}Sb_2$ ($x = 0.2$, 0.5, 0.8) crystals, we employed neutrons with a wavelength of 1.542 Å involving 1.4% λ/2 contamination from the Si-220 monochromator using its high resolution mode (bending 150)[26]. The crystal and magnetic structures were investigated in different temperature windows. The order parameter of a few important nuclear and magnetic peaks was measured. Data were recorded over a temperature range of $4 < T < 340$ K using a closed-cycle refrigerator available at the FCD. Due to the involvement of the high-absorbing europium in the $Eu_{1-x}Sr_xMn_{1-z}Sb_2$ crystals, proper neutron absorption corrections to the integrated intensities of the nuclear/magnetic peaks are indispensable. The dimensions of the faces for each crystal were measured, and a face index absorption correction of the integrated intensities was conducted carefully using the WinGX package[27]. The SARAh representational analysis program[28] and Bilbao crystallographic server[29] were used to derive the symmetry-allowed magnetic structures and magnetic space groups. The full datasets at different temperatures were analyzed using the refinement program FullProf suite[30] to obtain the structure and magnetic structures.

### Magnetization and magnetotransport measurements

The temperature and field dependence of the magnetization were measured in a superconducting quantum interference device magnetometer (Quantum Design) in magnetic fields up to 7 T. The transport measurements at zero magnetic field were performed with a four-probe method using Physical Property Measurement Systems (PPMS). The high-field magnetotransport properties were measured in 31 T resistivity magnets at the National High Magnetic Field Laboratory (NHMFL) in Tallahassee. The magnetic fields were applied parallel to the out-of-plane direction to study the in-plane and out-of-plane magnetoresistance. The $\rho_{in}$ samples were made into Hall bar shapes, and the $\rho_{out}$ samples were in the Corbino disk geometry. The Berry phase was extracted from the Landau fan diagram. The integer Landau levels are assigned to the magnetic field positions of resistivity minima in SdH oscillations, which correspond to the minimal density of state.

## Results and discussion

### Crystal structures

Both single-crystal X-ray and neutron diffraction reveal that the parent compound $EuMnSb_2$ crystallizes in a tetragonal structure with space group *P4/nmm* (Figs. 1a and S1e) and nonstoichiometric composition $EuMn_{0.95}Sb_2$. The structural parameters of $EuMn_{0.95}Sb_2$ obtained from the single-crystal X-ray diffraction refinement at 293 K are summarized in Tables SI and SII. Note that the structure of $EuMn_{0.95}Sb_2$ is similar to that of $CaMnBi_2$[31] but different from the *I4/mmm* in the tetragonal structure of $EuMnBi_2$[16] and the previously reported orthorhombic structure of $EuMnSb_2$[17,19]. The energy-dispersive X-ray spectroscopy analysis shows that there are also less than 5% Mn deficiencies in the Sr-doped compounds with $z\sim0.01$, 0.05, and 0.02 for $x = 0.2$, 0.5, and 0.8, respectively.

Interestingly, the Sr-doped $Eu_{1-x}Sr_xMn_{1-z}Sb_2$ ($x = 0.2$, 0.5, and 0.8) shows a clear lattice distortion and crystallizes in the orthorhombic structure with the space group *Pnma*, with a doubled unit cell along the out-of-plane direction (Figs. 1b, c and S1f), similar to $SrMnSb_2$[6]. Thus, the Sr doping at the Eu site in $EuMn_{0.95}Sb_2$ induces symmetry breaking from tetragonal *P4/nmm* to *Pnma*. Our systematic studies on Sr-doped $EuMn_1-zSb_2$ and comparison with previous reports on the parent compound suggest that the structural difference between our $x = 0$ sample and the samples reported in the literature[17,19] arises from the nonstoichiometric compositions and/or flux-induced chemical doping. The sample reported in ref. [17] involves Sn doping at the Sb sites due to the use of Sn flux, which yields a composition of $Eu_{0.992}Mn_{1.008}Sb_{1.968}Sn_{0.73}$. In ref. [19], the composition was reported to be $EuMn_{1.1}Sb_2$, which implies that a significant amount of Mn antisite defects may exist at the Sb sites. In contrast, our parent compound $x = 0$ is characterized by only a small degree of Mn deficiency. Such composition differences from the previously reported samples explain why our $x = 0$ sample is tetragonal, whereas the samples reported in the literature are orthorhombic. This also indicates that chemical doping at the Eu, Mn, or Sb sites in $EuMnSb_2$ could induce orthorhombic distortion.

The structural parameters of $Eu_{1-x}Sr_xMn_{1-z}Sb_2$ ($x = 0$, 0.2, 0.5, and 0.8) at 5 K obtained from the fits to neutron diffraction data are summarized in Table 1. It can be seen that Sr doping induces a slight decrease in the out-of-plane lattice constant and an increase in the in-plane lattice constants. More details about the determination of crystal structures of all the $Eu_{1-x}Sr_xMn_{1-z}Sb_2$ compounds can be found in the Supplemental Information.

### Determination of magnetic structures

In general, determining the complicated magnetic structures in Eu-containing compounds is difficult due to the strong neutron absorption of europium. Proper neutron absorption correction of the neutron diffraction

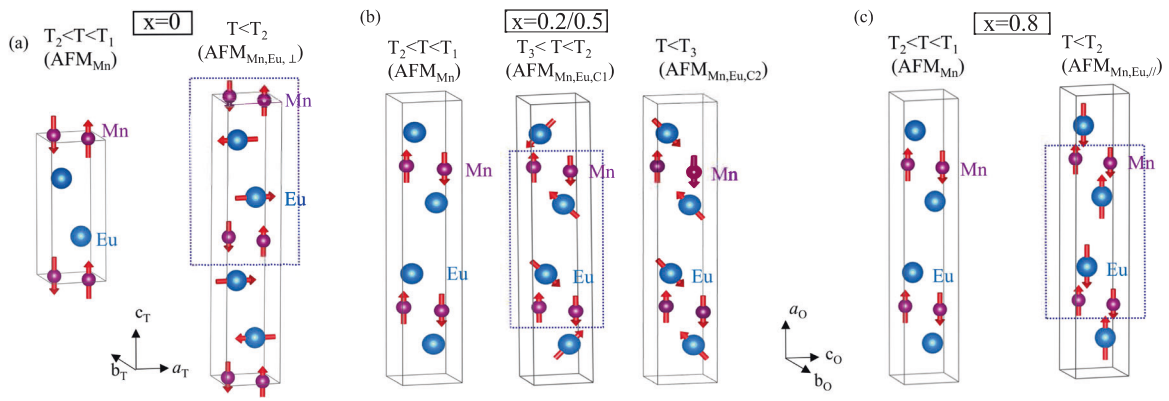


**Fig. 1 Magnetic structures of $Eu_{1-x}Sr_xMn_{1-z}Sb_2$.** Magnetic structures determined from the fits to the neutron data for **a** $x = 0$, **b** $x = 0.2$ (all the panels) and 0.5 (only left and middle panels), and **c** $x = 0.8$. The dashed rectangle shows the Mn–Eu–Eu–Mn block where the SR of Eu can be seen.

**Table 1 Structural parameters of $Eu_{1-x}Sr_xMn_{1-z}Sb_2$ with $x = 0$, 0.2, 0.5, and 0.8 at 5 K obtained through the fitting of the single-crystal neutron diffraction data. For $x = 0$, space group: *P4/nmm*. Atomic positions: Eu(2c): (0.25, 0.25, *z*), Mn(2a): (0.75, 0.25, 0), Sb1(2b): (0.75, 0.25, 0.5), Sb2(2c): (0.25, 0.25, *z*). For $x > 0$ compounds: Space group: *Pnma*. Eu/Sr(4c): (*x*, 0.25, *z*), Mn(4c): (*x*, 0.25, *z*), Sb1(4c):(*x*, 0.25, *z*), Sb1(4c): (*x*, 0.25, *z*).**

| | | | $x = 0$ | | $x = 0.2$ | $x = 0.5$ | $x = 0.8$ |
|---|---|---|---|---|---|---|---|
| Lattice constants | | | | | | | |
| | *a* | | 4.343 (6) | | 22.348 (3) | 22.27 (42) | 22.28 (41) |
| | *b* | | 4.343 (6) | | 4.347 (5) | 4.411 (14) | 4.412 (14) |
| | *c* | | 11.169 (13) | | 4.383 (4) | 4.434 (24) | 4.438 (28) |
| | Atom | | | | | | |
| Eu | | *z* | 0.729(5) | *x* | 0.113 (4) | 0.113 (5) | 0.112 (4) |
| | | | | *z* | 0.781 (5) | 0.789 (7) | 0.806 (3) |
| | Mn | | | *x* | 0.253 (7) | 0.249 (4) | 0.242 (4) |
| | | | | *z* | 0.323 (3) | 0.279 (7) | 0.292 (4) |
| | Sb1 | | | *x* | 0.0019 (8) | 0.0011 (7) | 0.0042 (9) |
| | | | | *z* | 0.233 (6) | 0.264 (4) | 0.298 (7) |
| Sb2 | | *z* | 0.156(7) | *x* | 0.324 (5) | 0.325 (5) | 0.324 (6) |
| | | | | *z* | 0.829 (5) | 0.768 (4) | 0.818 (5) |
| Reliable factors | | | | | | | |
| | Rf | | 8.75 | | 6.67 | 6.18 | 7.59 |
| | $_{\chi}2$ | | 0.28 | | 0.28 | 1.21 | 0.83 |

data is critical. We employed single-crystal neutron diffraction to solve the complicated magnetic structures of $Eu_{1-x}Sr_xMn_{1-z}Sb_2$ below 340 K. The refined moments, Mn–Eu canting angle, and reliability factors of the refinements of the neutron data after neutron absorption correction are summarized in Table 2 (see the Supplemental Information for more details).

Figure 2a–d shows the temperature dependences of a few representative nuclear and/or magnetic reflections of $Eu_{1-x}Sr_xMn_{1-z}Sb_2$. For the $x = 0$ parent compound, the presence of the pure magnetic peak at $(100)_T$ below $T1$ at 330 K indicates one magnetic transition. The absence of an anomaly at $T_1$ in susceptibility measurements (see Fig. 3a) may be ascribed to the possible strong spin fluctuations above $T_1$ that tend to smear out any anomalies in the susceptibility as in other Mn-based compounds[6,20,22]. For $T < T_1$, a C-type AFM order of Mn spins ($AFM_{Mn}$) with the propagation vector $\boldsymbol{k} = (0,0,0)_T$ and the moment along the $c_T$ axis is determined without Eu ordering, as illustrated in the left panel of Fig. 1a. Upon cooling below $T_2$ at 22 K, there is an increase in magnetic peak intensities such as $(100)_T$ and $(101)_T$ with $\boldsymbol{k} = (0,0,0)_T$ and, simultaneously, new magnetic reflections with a propagation vector $\boldsymbol{k} = (0,0,1/2)_T$ from the Eu sublattice appear.

Interestingly, we observed strong magnetic peaks (0, 0, $L/2)_T$ ($L$ = odd number) below $T_2$ (see the inset of Fig. 2a). This excludes the possibility of Eu moments pointing in the out-of-plane axis seen in $EuMnBi_2$[16,32]. The determined magnetic structure for $T < T_2$ denoted by $AFM_{Mn, Eu,\perp}$ is shown in the right panel of Fig. 1a. Whereas Mn preserves a C-type AFM order with an increased moment due to Eu-Mn coupling along the $c_T$ axis, the "+ + − −" Eu spin ordering with the moment along the $a_T$ axis breaks the magnetic symmetry along the $c_T$ axis and leads to observed magnetic reflections with $\boldsymbol{k} = (0,0,1/2)_T$. Such a magnetic structure is consistent with the susceptibility measurements in Fig. 3a, where $\chi_c$ increases slightly and $\chi_{ab}$ decreases rapidly for $T < T_2$, suggesting an AFM moment oriented along the $a_Tb_T$ plane. Note that the magnetic structure determined here is different from the "+-+-" A-type Eu order proposed on the basis of diffraction experiments on a polycrystalline sample of $EuMnSb_2$, for which no $\boldsymbol{k} = (0,0,1/2)_T$ magnetic peaks were observed below $T_2$. The Eu moment canting proposed in ref. [19] is not found in our crystal for $T < T_2$ (see the Supplemental Information for a detailed discussion).

In the $x = 0.2$ compound, the temperature dependence of the pure magnetic peak $(010)_O$ in the orthorhombic structure, corresponding to the $(100)_T$ in the tetragonal notation, shows a clear magnetic transition at the $T_1$ of 330 K, as shown in Fig. 2b. A similar C-type AFM order ($AFM_{Mn}$) with $\boldsymbol{k} = (0,0,0)_O$ was determined and is displayed in the left panel in Fig. 1b. Upon cooling below $T_2$ at 21 K, new magnetic peaks indexed by ($H$, $K$, $L$) ($H$ = odd integers), for instance $(700)_O$, corresponding to (0 0 $3.5)_T$, are observed (see inset of Fig. 2b). All the magnetic peaks can be described by the AFM order at $k = (0,0,0)_O$ in the orthorhombic notation due to the doubled unit cell in contrast to $x = 0$. Within the temperature range of $T_3 < T < T_2$, we find a canted and noncollinear Eu spin order confined within the $a_Oc_O$ plane with a "+ + − −' component along the $c_O$ axis and a "+ − + −" component along the $a_O$ axis, coexisting with the C-type Mn AFM order with moments along the $a_O$ axis (denoted by $AFM_{Mn,Eu,C1,}$ the middle panel in Fig. 1b). This is consistent with the susceptibility measurement shown in Fig. 3b, where both $\chi_a$ and $\chi_{bc}$ decrease below $T_2$, implying that Eu spins may form a canted AFM order. Note that such a canted Eu order is not applicable in the corresponding $T < T_2$ temperature region of the $x = 0$ parent compound. At 10 K, the canting angle between Mn and Eu is 41(9)°. The susceptibility measurements show that $\chi_a$ increases but $\chi_{bc}$ decreases anomalously below $T_3$ at 7 K, indicative of another magnetic transition. Interestingly, there is a decrease in the $(300)_O$ peak intensity, with a concurrent increase in the intensity of the nuclear peak

**Table 2 Refined magnetic moments, Mn–Eu angles, and reliable factors of $Eu_{1-x}Sr_xMn_{1-z}Sb_2$ with $x = 0$, 0.2, 0.5, and 0.8 at different temperatures.**

| | | $x = 0$ | | $x = 0.2$ | | | $x = 0.5$ | | $x = 0.8$ |
|---|---|---|---|---|---|---|---|---|---|
| | $T$ (K) | 170 | 5 | 60 | 10 | 4 | 50 | 5 | 5 |
| Mn moments | $M_c(x = 0)$ | 2.99 (29) | 4.63 (21) | | | | | | |
| | $M_a(x > 0)$ | | | 3.70 (46) | 3.66 (32) | 3.75 (45) | 3.74 (15) | 3.76 (17) | 3.80 (22) |
| Eu moments | $M_a$ | | | | 4.08 (34) | 3.89 (69) | | 4.84 (55) | 5.17 (62) |
| | $M_c$ | | 5.25 (43) | | 3.52 (34) | 3.30 (86) | | 2.23 (29) | |
| | $\lvert M_{total}\rvert$ | | 5.25 (43) | | 5.38 (34) | 5.26 (50) | | 5.32 (50) | 5.17 (62) |
| Mn–Eu moment angle(°) | | | 90 (7) | | 41 (9) | 40 (7) | | 24 (8) | 0 |
| Reliable factors | RF ($\boldsymbol{k}$ = (0, 0, 0)) | 9.53 | 8.75 | 7.64 | 7.55 | 6.67 | 5.32 | 6.18 | 7.59 |
| | $\chi^2$($\boldsymbol{k}$ = (0, 0, 0)) | 0.27 | 0.28 | 0.13 | 0.29 | 0.28 | 0.31 | 1.26 | 0.83 |
| | RF ($\boldsymbol{k}$ = (0, 0, 1/2)) | | 8.93 | | | | | | |
| | $\chi^2$($\boldsymbol{k}$ = (0, 0, 1/2)) | | 0.26 | | | | | | |

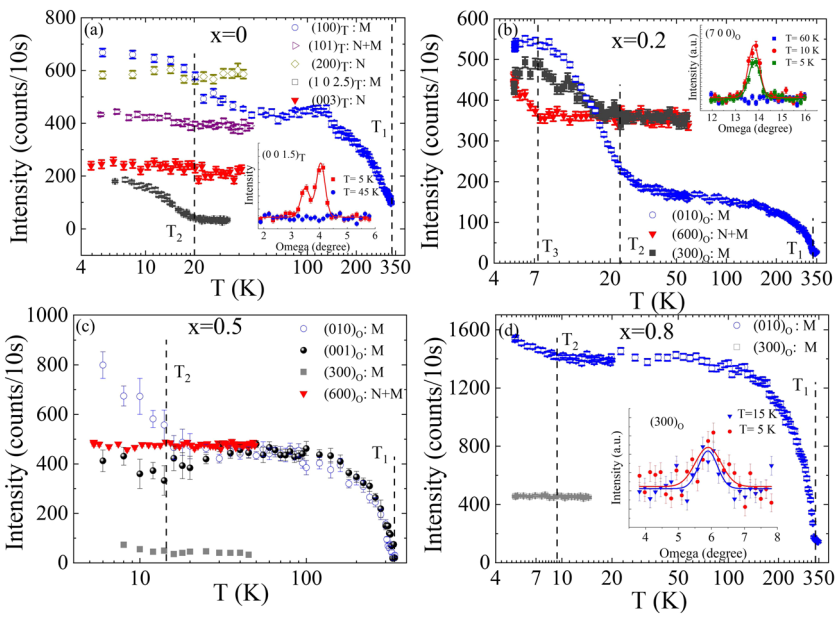


**Fig. 2 Neutron results on nuclear and magnetic peaks of $Eu_{1-x}Sr_xMn_{1-z}Sb_2$.** Temperature dependence of intensities at the representative nuclear and/or magnetic peak positions for **a** $x = 0$, **b** $x = 0.2$, **c** $x = 0.5$, and **d** 0.8. The insets show a comparison of the nuclear/magnetic peaks at different temperatures. The 2nd weak peak with a smaller omega in the rocking curves for $x = 0$ is due to the presence of another tetragonal domain rather than an orthorhombic domain in the crystal. The very weak (300) peak in **d** results from the $\lambda/2$ contamination of neutrons. The vertical lines indicate the locations of the magnetic transition temperatures.

$(600)_O$ for $T < T_3$. This strongly indicates a Eu spin-reorientation transition to a Eu spin order without magnetic symmetry breaking along the $a_O$ axis. When the C-type Mn order is unchanged, a canted and collinear magnetic structure with A-type "+ − + −" Eu spin order along both the $a_O$ and $c_O$ axes ($AFM_{Mn,Eu,C2}$) occurs with a Mn–Eu canting angle of 40(7)° at 4 K, as shown in the right panel of Fig. 1b. At 4 K, the Mn and Eu moments are found to be 3.75(45) and 5.26(50) $\mu_B$, respectively, indicative of $Mn^{2+}$ ($S = 5/2$) and $Eu^{2+}$ ($S = 7/2$).

When $x$ is increased to 0.5 or 0.8, the Eu lattice exhibits only a single AFM transition as revealed from the

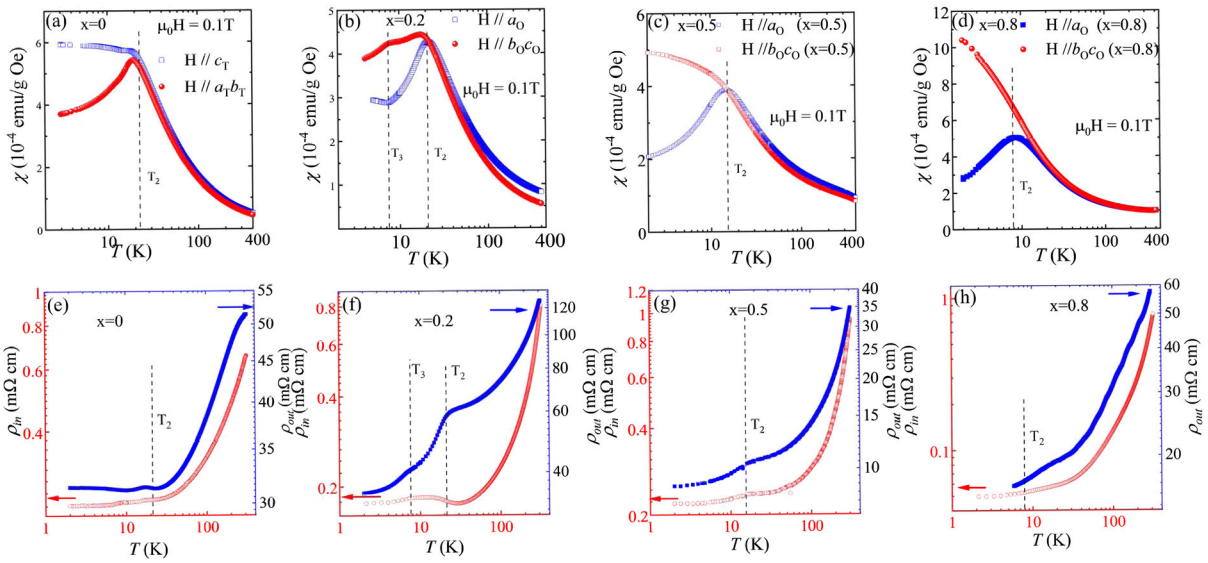


**Fig. 3 Susceptibility and resistivity of $Eu_{1-x}Sr_xMn_{1-z}Sb_2$.** Temperature dependence of the susceptibility of **a** $x = 0$ with a magnetic field of 0.1 T parallel to the out-of-plane $c_T$ and in-plane $a_T b_T$ directions and **b** $x = 0.2$, **c** $x = 0.5$, and **d** $x = 0.8$ with the field parallel to the out-of-plane $a_O$ and in-plane $b_O c_O$ directions. Temperature dependence of the out-of-plane resistivity $\rho_{out}$ and in-plane longitudinal resistivity $\rho_{in}$ at zero magnetic field for **e** $x = 0$, **f** $x = 0.2$, **g** $x = 0.5$ and **h** $x = 0.8$.

susceptibility measurements shown in Fig. 3c, with $T_2$ at 17 K for $x = 0.5$ and 8 K for $x = 0.8$. For the $x = 0.5$ sample, both the $(010)_O$ and $(001)_O$ magnetic peaks appear below $T_1$. Upon cooling below $T_2$ at 15 K, the $(010)_O$ peak intensity further increases, while there is no obvious change in the $(001)_O$ peak (see Fig. 2c and Fig. S5a, b). Furthermore, there is an increase in the peak intensity $(300)_O$ due to the magnetic contribution but no obvious change in the peak intensities of $(200)_O$ or $(600)_O$. These features are similar to those at $x = 0.2$. We indeed obtain similar magnetic structures in the $x = 0.5$ sample, as shown in the left panel ($AFM_{Mn}$) and middle panel ($AFM_{Mn,Eu,C1}$) in Fig. 1b for $T_2 < T < T_1$ and $T_3 < T < T_2$, respectively. Note that the canting angle between Eu and Mn moments decreases to 24(8)° at 5 K.

As x increases to 0.8, the Mn magnetic transition occurs at a $T_1$ of 330 K as identified from the intensity of $(010)_O$, and a C-type Mn order $AFM_{Mn}$ is determined (see the left panel of Fig. 1c). Another increase in $(010)_O$ is found below $T_2 \approx 7$ K. There is no appearance of magnetic scattering at the $(300)_O$ and $(200)_O$ or $(600)_O$ Bragg positions below $T_2$ (see the inset of Fig. 2d and Fig. S5c in SI), indicating that Eu moments may point to the $a_O$ axis. We find a coexistence of C-type Mn AFM order with the "+ − + −" Eu order with an oriented moment along the same $a_O$ axis as the Mn moment ($AFM_{Mn,Eu,}$, see the right panel of Fig. 1c), consistent with susceptibility measurements. As shown in Fig. 3d, $X_{bc}$ keeps increasing, but $X_a$ decreases rapidly upon cooling below 8 K, showing behavior opposite to that of $x = 0$. This indicates that the Eu moment mainly points in the out-of-plane $a_O$ direction at $x = 0.8$.

## Electronic transport properties

Next, we present the evolution of the electronic transport properties with Sr doping in $Eu_{1-x}Sr_xMn_{1-z}Sb_2$. As shown in Fig. 3e–h, both the in-plane longitudinal resistivity $\rho_{in}$ and out-of-plane resistivity $\rho_{out}$ exhibit metallic transport properties. At 2 K, $\rho_{out}/\rho_{in}$ reaches 128, 198 and 322 for $x = 0$, $x = 0.2$ and $x = 0.8$, respectively. Such a rapid increase in electronic anisotropy indicates that Sr doping reinforces the quasi-2D electronic structure. In the $x = 0$ sample (see Figs. 3e and S7a), the slope of $\rho_{out}$ and $\rho_{in}$ decreases below $T_2$, indicative of the coupling between the emergence of Eu order and the transport properties, suggesting that the in-plane Eu "+ + - -" order leads to suppressed metallicity. The metallic behavior in our $EuMn_{0.95}Sb_2$ sample is different from the insulating behavior observed in the Sn- or Mn-doped nonstoichiometric samples[17,19]. This indicates that chemical doping at Sb or Mn sites induces a metal-insulator transition that is distinct from the effect of Sr substitution for Eu.

However, the $x = 0.2$ sample exhibits transport behavior distinct from that of the $x = 0$ sample. We observe a rapid decrease in $\rho_{out}$ and a slight increase in $\rho_{in}$ below $T_2$ (see Figs. 3f and S7b), suggesting that the Eu canting to the $a_O$ axis with the Eu "+ − + −" component significantly increases the interlayer conductivity along the $a_O$ direction between Sb layers but suppresses the intralayer conductivity on the $b_O c_O$ plane, in contrast with the effect

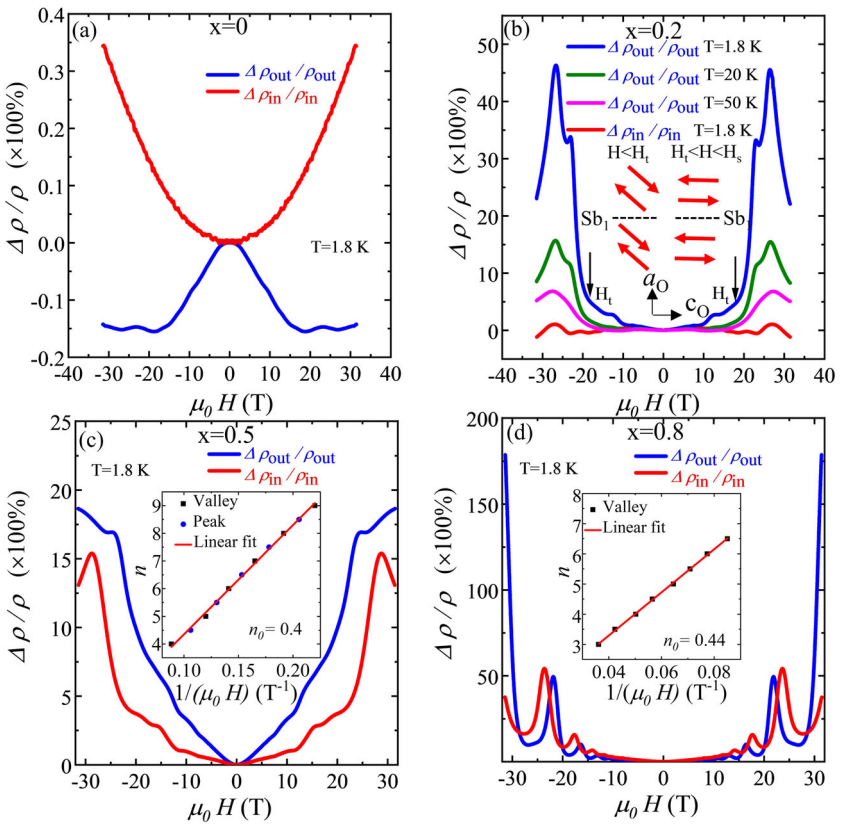


**Fig. 4 High field magnetoresistance of $Eu_{1-x}Sr_xMn_{1-z}Sb_2$.** Field dependence of the out-of-plane magnetoresistance $\Delta\rho_{out}/\rho_{out}$ and in-plane magnetoresistance $\Delta\rho_{in}/\rho_{in}$ for **a** $x = 0$, **b** $x = 0.2$, **c** $x = 0.5$, and **d** $x = 0.8$. The inset of **b** shows the field-induced metamagnetic transition in the Eu sublattice, i.e., Eu spin ordering in and $H < H_f$ and $H_f < H < H_s$. The insets of **c**, **d** show the linear fit of the Landau level fan diagram based on both the oscillatory resistivity $\rho_{in}$ and the second derivative of the resistivity $-d^2\rho_n/dB^2$ for $x = 0.5$ and based on only the oscillatory resistivity $\rho_{in}$ for $x = 0.8$.

of the sole in-plane Eu order on the transport properties described above. Below $T_3$, there are no obvious changes in the out-of-plane resistivity, but an anomalous decrease in the in-plane resistivity is observed. This can be attributed to the SR of Eu from noncollinear to collinear order. Below $T_3$, the out-of-plane Eu order is kept at "+ − + −", which is not expected to influence the interlayer conductivity. In contrast, the switch of the in-plane component from "+ + − −" to "+ − + −" induces an anomalous increase in the intralayer conductivity.

When x increases to 0.5, the "+ − + −" component of the Eu order along the $a_O$ axis direction also induces an increase in the interlayer conductivity below $T_2$ (see Figs. 3g and S7c), but the increase is weaker than that at $x = 0.2$. Furthermore, the weak decrease in the intralayer conductivity at $x = 0.2$ is hardly observed near $T_2$ at $x = 0.5$. Both are ascribed to the reduction in Eu occupancy to ≈ 50% at $x = 0.5$, which weakens the effect of Eu order on the transport properties. For $x = 0.8$, the Eu ordering does not obviously influence the resistivity below $T_2$, as shown in Figs. 3h and S7d, which can be ascribed to the low Eu occupancy (≈ 20%). Thus, our results reveal an intimate coupling between the Eu magnetic order and transport properties in $Eu_{1-x}Sr_xMn_{1-z}Sb_2$.

## Nontrivial Berry phases

Figure 4a–d shows both in-plane and out-of-plane magnetoresistance (MR = $[\rho\ (B) - \rho\ (0)]/\rho\ (0)$) under high magnetic fields applied along the out-of-plane direction. For $x = 0$, $\Delta\rho_{out}/\rho_{out}$ is negative, whereas the in-plane $\Delta\rho_{in}/\rho_{in}$ is positive. The magnitudes for both $\Delta\rho_{out}/\rho_{out}$ and $\Delta\rho_{in}/\rho_{in}$ are small, and no strong Shubnikov-de Haas (SdH) oscillations are observed. For $x = 0.2$, weak SdH oscillations are observed in both $\Delta\rho_{out}/\rho_{out}$ and $\Delta\rho_{in}/\rho_{in}$. As the field increases, there is a sign reversal in $\rho_{in}/\rho_{in}$, whereas $\Delta\rho_{out}/\rho_{out}$ remains positive. Remarkably, at 1.8 K, which is below $T_3$, a large jump in $\Delta\rho_{out}/\rho_{out}$ up to 4500% occurs above a $\mu_0 H_t$ of 18 T. The dramatic changes in $\Delta\rho_{out}/\rho_{out}$ near $\mu_0 H_t$ of 18 T are ascribed to a field-induced metamagnetic transition. Since this phenomenon does not occur in the $T > T_2$ temperature regime (e.g., 50 K), the field-induced magnetic transition does not originate from the Mn magnetic sublattice but is related to the Eu magnetic sublattice, which is

indicative of the vital role that the Eu magnetic order plays in the magnetotransport properties. The most likely origin of the enhanced $\Delta\rho_{out}/\rho_{out}$ above $\mu_0 H_t$ of 18 T is the field-induced Eu SR transition from the canted moment direction in the $a_O c_O$ plane to the $c_O$ axis, while the A-type "+ − + −" Eu order remains, thus strongly suppressing interlayer conductivity, as illustrated in the inset of Fig. 4b. Note that this is different from the field-induced spin-flop transition of the "+ + − −" Eu order from the out-of-plane $c_O$ axis to the in-plane direction in $EuMnBi_2$[16]. Above ~ 28 T, the rapid decrease in $\Delta\rho_{out}/\rho_{out}$ may indicate the full polarization of Eu spins to the external field direction, i.e., the $a_O$ axis, similar to the scenario seen in $EuMnBi_2$[16]. Further high-field magnetization measurements are required to confirm these metamagnetic transitions.

An increase in the Sr doping level significantly enhances SdH oscillations in both $\Delta\rho_{out}/\rho_{out}$ and $\Delta\rho_{in}/\rho_{in}$ for $x = 0.5$ and 0.8, respectively, with much higher oscillation amplitudes at high magnetic fields. $\Delta\rho_{out}/\rho_{out}$ reaches ≈ 18,000% at 31.5 T for $x = 0.8$. We further analyze the Berry phase (BP) $\phi_B$ accumulated along cyclotron orbits and are able to extract $\phi_B$ for $x = 0.5$ and 0.8. Based on the field dependence data of $\rho_{in}$ measured in a 14 T PPMS, which show well-resolved SdH oscillations in Fig. S8a, we obtain the second derivative of resistivity $-d^2\rho_{in}/dB^2$ and the oscillatory component of $\rho_{in}$ after background subtraction. The oscillation peaks and valleys obtained from both analyses are well-matched, as shown in Fig. S8b. With six oscillation valleys assigned to integer Landau levels (LLs) and five peaks assigned to half integer LLs, a Landau index fan diagram can be established, from which a nontrivial Berry phase of 0.8 $\pi$ can be unambiguously extracted, as displayed in the inset of Fig. 4c. As shown in Fig. 4d, we extract a Berry phase of 0.88 $\pi$ for the $x = 0.8$ compound. The Berry phases in both the $x = 0.5$ and 0.8 samples are apparently close to an ideal Berry phase for a quasi-2D system. The nontrivial Berry phase provides evidence that $x = 0.5$ and 0.8 harbor relativistic Dirac fermions. Our results clearly show that the substitution of Eu by nonmagnetic Sr induces Dirac semimetallic behavior that is closely associated with the controllable Eu magnetic order.

Unlike the $x = 0.2$ sample, the $x = 0.5$ and 0.8 samples do not show large jumps in $\rho_{out}/\rho_{out}$ in the field up to 31 T. This indicates the absence of field-induced metamagnetic transitions in both compounds. Therefore, the nontrivial Berry phase may be intrinsic for $x = 0.5$ and 0.8 compounds. In addition, compared to $SrMnSb_2$, with only an ordered Mn moment, the $x = 0.5$ and 0.8 samples exhibit distinct Eu orders coexisting with Mn orders, and the increase in Eu canting angle is accompanied by stronger quantum oscillations.

## Composition phase diagram

From the combination of single-crystal X-ray diffraction, neutron diffraction, magnetization, and magnetotransport measurements, we are able to establish the structural, magnetic, and electronic phase diagram, as illustrated in Fig. 5. While the $x = 0$ parent compound with Mn deficiency is tetragonal with the space group *P4/mmm*, Sr doping induces an orthorhombic distortion. This is consistent with previous reports on the orthorhombic structure in doped nonstoichiometric samples[17,19]. Notably, our $EuMn_{0.95}Sb_2$ sample forms a magnetic structure with perpendicular Mn and Eu moments at the ground state and does not exhibit topological semimetallic behavior, different from previous reports on samples with different compositions[17–19]. Sr substitution for Eu in $EuMnSb_2$ induces a slight decrease in $T_1$ but suppresses $T_2$ significantly. Furthermore, an increase in Sr concentration drives an unusual Eu SR from the in-plane to the out-of-plane direction and simultaneously induces the appearance of Dirac semimetallic behaviors. A higher Eu canting angle characterized by a smaller Eu–Mn angle is accompanied by stronger quantum SdH oscillations. Our results show that Eu spin canting can be driven by chemical doping, which could explain the observation of Eu canting in a doped

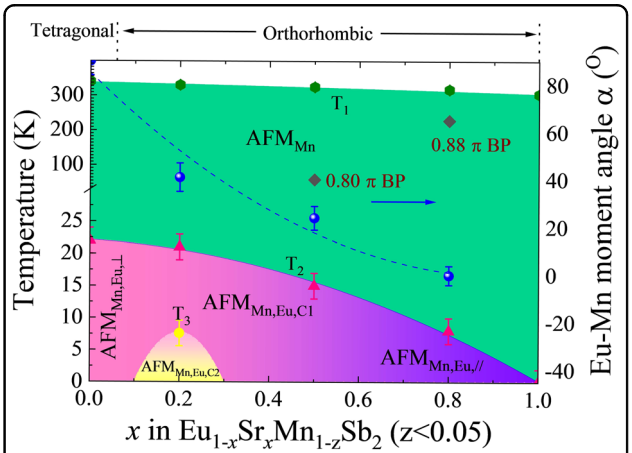


**Fig. 5 Composition phase diagram of $Eu_{1-x}Sr_xMn_{1-z}Sb_2$ with the structural and magnetic transitions, Eu–Mn moment angle α and nontrivial Berry phase (BH) extracted from the fits to $\rho_{in}$.** $T_1$, $T_2$, and $T_3$ label the magnetic transition temperatures. The distinct magnetic structures ($AFM_{Mn}$, $AFM_{Mn,Eu,\perp}$, $AFM_{Mn,Eu,C1}$, $AFM_{Mn,Eu,C2}$, and $AFM_{Mn,Eu,//}$) are displayed in Fig. 1b–d. $AFM_{Mn,Eu,//}$ and $AFM_{Mn,Eu,\perp}$ indicate the parallel and perpendicular moments of Mn and Eu, respectively. $AFM_{Mn,Eu,C1}$ and $AFM_{Mn,Eu,C2}$ show the two distinct canted moments between Mn and Eu. The evolution of the violet color illustrates the gradual decrease in the Eu–Mn moment angles. A higher Eu canting angle of $(90^\circ - \alpha)$, i.e., a smaller α, is accompanied by stronger quantum SdH oscillations. All the compounds exhibit metal-like transport properties as a function of temperature, and they are also coupled to the Eu order at $T_2$ and $T_3$. The nontrivial Berry phases indicative of Dirac semimetallic behaviors emerge for $x \geq 0.5$.

nonstoichiometric sample[19]. Note that no other magnetic transition is observed at $T_3$ in ref. [19] For our $x = 0.2$ compound, a 2nd type of Eu SR from a noncollinear canted spin order to a collinear A-type canted spin order is found at lower temperature (denoted by $AFM_{Mn,Eu,C2}$ in Fig. 5). Furthermore, the Eu order at the base temperature can be easily tuned by the external magnetic field to another type of SR, leading to a canted AFM state with the moments oriented to the possible $c_O$ axis. The established phase diagram for $Eu_{1-x}Sr_xMn_{1-z}Sb_2$ as well as the comparison with the previous reports we made above[17–19] indicate that the structure, magnetic order, and electronic properties of $EuMnSb_2$ are easily perturbed by chemical doping at any of the Eu, Mn, and Sb sites, indicating that the lattice, spin and charge degrees of freedom are strongly coupled in this material. This could account for the conflicting results reported in the literature[17–19] regarding the structure, magnetic, and electronic transport properties of $EuMnSb_2$ and implies that the nonstoichiometry must be taken into account to understand the intrinsic crystal and magnetic structure and magnetotransport properties of $EuMnSb_2$.

While chemical doping at Sb or Mn sites[17,19] in nonstoichiometric samples induces a tetragonal-orthorhombic structural transition, as in our $Eu_{1-x}Sr_xMn_{1-z}Sb_2$ ($x > 0$), such doping induces a metal–insulator transition yielding insulating behavior. This indicates that doping at the Sb or Mn sites may be detrimental to forming semimetallic behavior in $EuMnSb_2$ derivatives. In contrast, our phase diagram clearly shows that Sr doping at the Eu site is the driving force of the Dirac semimetallic behavior in $Eu_{1-x}Sr_xMn_{1-z}Sb_2$, as discussed below. First, Sr doping at the Eu site lowers the lattice symmetry and modifies the structural parameters, as summarized in Table 1, which could in turn change the electronic band structure. Second, the different types of Eu spin reorientations driven by Sr doping, temperature, or magnetic field significantly influence the electronic transport and magnetotransport properties, indicating that the band structure is sensitively dependent on the magnetism of the Eu sublattice. As such, the phase diagram presented in Fig. 5 offers an excellent opportunity to explore the intimate interplay between the band relativistic effect and magnetism.

### Origin of various Eu spin reorientations

Finally, we discuss the origins of the complicated magnetic structures, in particular, the Sr-doping and temperature-induced Eu SR transition in $Eu_{1-x}Sr_xMn_{1-z}Sb_2$. A common SR in rare earth elements occurs because the rare earth element drives the Mn moment parallel to its moment direction once the rare earth spins are ordered with preferred in-plane orientation at low temperatures, as reported for several compounds such as RMnAsO (R = Nd or Ce)[20,21] and RMnSbO (R = Pr or Ce)[22,23]. However, Sr doping in $Eu_{1-x}Sr_xMn_{1-z}Sb_2$ generates a novel Eu SR where the moment changes from the in-plane direction to the out-of-plane direction while the Mn moment direction remains along the out-of-plane $a_O$ axis.

The $Mn^{2+}$ moment, which commonly displays very weak single-ion anisotropy as expected for the L = 0 of $Mn^{2+}$ ($S = 5/2$), favors orientation along the out-of-plane direction[20–22], i.e., the $c_T$ axis in the tetragonal structure or the $a_O$ axis in the orthorhombic structure, forming C-type AFM order in $T_2 < T < T_1$ of $Eu_{1-x}Sr_xMn_{1-z}Sb_2$. The in-plane checkerboard-like AFM structure of the C-type order suggests that the NN interaction $J_1$ is dominant, whereas the in-plane next-nearest-neighbor (NNN) interaction $J_2$ is very weak. In the context of the $J_1$–$J_2$–$J_c$ model[33], we conclude that $J_1 > 0$, $J_2 < J_1/2$ and out-of-plane $J_c < 0$ with negligible spin frustration in the Mn sublattice. Upon cooling to $T < T_2$, Eu-Eu coupling starts to come into play and induces Eu ordering with a preferred orientation of $Eu^{2+}$ ($S = 7/2$) in plane[34,35], either the $a_Tb_T$ plane in the tetragonal structure or the $b_Oc_O$ plane in the orthorhombic structure. Simultaneously, the Eu–Mn coupling also plays an important role by exerting an effective field that has the tendency to influence the Mn/Eu moment directions. The increase in Sr concentration on the Eu site weakens Eu–Eu coupling and destabilizes the preferred orientation of the Eu spins. Thus, as $x$ increases to 0.2, the effective field from Eu–Mn coupling tends to drive the Eu moment toward the Mn moment direction. The competition of Eu–Eu and Eu–Mn couplings induces spin frustration in the Eu sublattice and leads to a canted Eu order with the moment in the *ac* plane stabilized in $T_3 < T < T_2$. An increase in Sr doping has a tendency to further drive the Eu moment tilt toward the $a_O$ axis due to weakened Eu–Eu coupling, as shown by a lower Eu–Mn angle for $x = 0.5$. As the Sr doping increases to 0.8, the Eu–Mn coupling overwhelms the weak Eu–Eu coupling, which leads to an SR of Eu to the same moment direction as the Mn moment. This could account for the unusual Eu SR induced by Sr doping. As the temperature decreases below $T_3$ for $x = 0.2$, a temperature-induced SR transition occurs. This may be ascribed to another type of Eu–Eu coupling that comes into play below $T_3$. This retains the "+ − + −" out-of-plane component but switches the in-plane component from "+ + − −" to "+ − + −", leading to a collinear A-type AFM order of Eu spins in $T < T_3$. Thus, the striking Eu spin reorientation driven by Sr doping and temperature indicates strong Eu–Mn (4*f*–3*d*) couplings and results from their competition with Eu–Eu couplings.

To summarize, we report the composition phase diagram of the crystal and magnetic structures and electronic transport properties of $Eu_{1-x}Sr_xMn_{1-z}Sb_2$ and the realization of tunable topological semimetallic behavior by controlling various spin reorientations by chemical substitution, temperature, and/or an external magnetic field.

The structure, magnetic order, and electronic properties of the parent $EuMnSb_2$ are easily perturbed by chemical doping, and therefore, the nonstoichiometry must be taken into account to determine its intrinsic structure and physical properties. While we found that nearly stoichiometric $EuMnSb_2$ is not a topological semimetal, doping of nonmagnetic Sr on the Eu site induces an intricate coupling between the structure, various Eu spin reorientations, and quantum transport properties, indicating that $Eu_{1-x}Sr_xMn_{1-z}Sb_2$ is a wonderful platform for the study of the interplay between magnetism and the topological properties of the electronic band structure. The present study may inspire a search for semimetallic states and interesting magnetic states in the large $AMnCh_2$ (A = rare earth elements, such as Ce, Pr, Nd, Sm; Ch = Bi/Sb) family and other layered compounds involving spatially separated rare earth and transition metal layers by tuning the competition of $4f$–$3d$ and A–A magnetic couplings.

#### Acknowledgements
Q.Z. J.L, A.P., and J.F.D. acknowledge the support for the materials preparation, measurements of the magnetization, transport and magnetotransport properties, and neutron scatting experiments from the US DOE under EPSCoR Grant No. DESC0012432 with additional support from the Louisiana board of regents. The use of the High Flux Isotope Reactor at Oak Ridge National Laboratory was supported by the U.S. Department of Energy, Office of Basic Energy Sciences, Scientific User Facilities Division. D.A.T. is sponsored by the DOE Office of Science, Laboratory Directed Research and Development Program (LDRD) of Oak Ridge National Laboratory, managed by UT-Battelle, LLC for the U.S. Department of Energy (Project ID 9566). A portion of this work was performed at the National High Magnetic Field Laboratory, which is supported by the National Science Foundation Cooperative Agreement No. DMR-1644779 and the State of Florida.

#### Author details
[1]Neutron Scattering Division, Oak Ridge National Laboratory, Oak Ridge, TN 37831, USA. [2]Department of Physics and Astronomy, Louisiana State University, Baton Rouge, LA 70803, USA. [3]Department of Physics and Engineering Physics, Tulane University, New Orleans, LA 70118, USA. [4]National High Magnetic Field Laboratory, Tallahassee, FL 32310, USA. [5]Shull Wollan Center, Oak Ridge National Laboratory, Oak Ridge, TN 37831, USA. [6]Quantum Science Center, Oak Ridge, TN 37831, USA. [7]Department of Physics, Pennsylvania State University, University Park, PA 16802, USA

#### Author contributions
Q.Z. and J.L. contributed equally to this paper. J.L. and Z.M. prepared and characterized the high-quality single crystals. A.P. conducted single-crystal X-ray measurements and data analysis on $x = 0$. Q.Z., H.C., J.D., and D.A.T. performed the neutron experiments. D.G. assisted with the high-field magnetotransport measurements, while J.L. and Z.M. analyzed the magnetization and magnetotransport data. Q.Z. analyzed the neutron data and wrote the paper with input from all the authors.

#### Competing interests
The authors declare no competing interests.

#### Publisher's note
Springer Nature remains neutral with regard to jurisdictional claims in published maps and institutional affiliations.

**Supplementary information** The online version contains supplementary material available at https://doi.org/10.1038/s41427-022-00369-5.

Received: 10 August 2021 Revised: 22 January 2022 Accepted: 2 February 2022
Published online: 11 March 2022

#### References
1. Xu, S.-Y. et al. Discovery of a Weyl fermion semimetal and topological fermi arcs. *Science* **349**, 613–617 (2015).
2. Lu, L. et al. Experimental observation of Weyl points. *Science* **349**, 622–624 (2015).
3. Lv, B. Q. et al. Experimental discovery of Weyl semimetal TaAs. *Phys. Rev. X* **5**, 031013 (2015).
4. Armitage, N. P., Mele, E. J. & Vishwanath, A. Weyl and Dirac semimetals in three dimensional solids. *Rev. Mod. Phys.* **90**, 15001 (2018).
5. Wan, X., Turner, A. M., Vishwanath, A. & Savrasov, S. Y. Topological semimetal and Fermi arc surface states in the electronic structure of pyrochlore iridates. *Phys. Rev. B.* **83**, 205101 (2011).
6. Liu, J. Y. et al. A magnetic topological semimetal $Sr_{1-y}Mn_{1-z}Sb_2$. *Nat. Mater.* **16**, 905 (2017).
7. Park, J. et al. Anisotropic Dirac fermions in a Bi square net of $SrMnBi_2$. *Phys. Rev. Lett.* **107**, 126402 (2011).
8. Nakatsuji, S., Kiyohara, N. & Higo, T. Large anomalous Hall effect in a non-collinear antiferromagnet at room temperature. *Nature* **527**, 212 (2015).
9. Chang, G. et al. Magnetic and noncentrosymmetric Weyl fermion semimetals in the RAlGe family of compounds (R = rare earth). *Nature* **527**, 212 (2015).
10. Liu, E. et al. Giant anomalous Hall effect in a ferromagnetic kagome-lattice semimetal. *Nat. Phys.* **14**, 1125 (2018).
11. Zhang, Q. et al. Unusual exchange couplings and intermediate temperature Weyl state in $Co_3Sn_2S_2$. *Phys. Rev. Lett.* **127**, 117201 (2021).
12. Sakai, A. et al. Giant anomalous Nernst effect and quantum-critical scaling in a ferromagnetic semimetal. *Nat. Phys.* **14**, 1119 (2018).
13. Belopolski, I. et al. Discovery of topological Weyl fermion lines and drumhead surface states in a room temperature magnet. *Science* **365**, 1278 (2019).
14. Wollesen, P., Jeitschko, W., Brylak, M. & Dietrich, L. Ternary antimonides $LnM_{1-x}Sb_2$ with Ln = La−Nd, Sm, Gd, Tb and M = Mn, Co, Au, Zn, Cd. *J. Alloy. Compd.* **245**, L5–L8 (1996).
15. Borisenko, S. et al. Time-reversal symmetry breaking type-II Weyl state in YbMnBi2. *Nat. Commun.* **10**, 3424 (2019).
16. Masuda, H. et al. Quantum Hall effect in a bulk antiferromagnet $EuMnBi_2$ with magnetically confined two-dimensional Dirac fermions. *Sci. Adv.* **2**, e1501117 (2016).
17. Yi, C. et al. Large negative magne-toresistance of a nearly Dirac material: Layered antimonide $EuMnSb_2$. *Phys. Rev. B* **96**, 205103 (2017).
18. Soh, J.-R. et al. Magnetic and electronic structure of Dirac semimetal candidate $EuMnSb_2$. *Phys. Rev. B* **100**, 174406 (2019).
19. Gong, D. et al. Canted Eu magnetic structure in $EuMnSb_2$. *Phys. Rev. B* **101**, 224422 (2020).
20. Zhang, Q., Tian, W., Peterson, S. G., Dennis, K. W. & Vaknin, D. Spin reorientation and Ce–Mn coupling in antiferromagnetic oxypnictide CeMnAsO. *Phys. Rev. B* **91**, 064418 (2015).
21. Emery, N. et al. Variable temperature study of the crystal and magnetic structures of the giant magnetoresistant materials LmnAsO (L = La, Nd). *Phys. Rev. B* **83**, 144429 (2011).
22. Zhang, Q. et al. Structure and magnetic properties of LnMnSbO (Ln = La and Ce). *Phys. Rev. B* **93**, 094413 (2016).
23. Kimber, S. A. J. et al. Local moments and symmetry breaking in metallic PrMnSbO. *Phys. Rev. B* **82**, 100412 (2010).
24. Altomare, A. et al. *SIR*97: A new tool for crystal structure determination and refinement. *J. Appl. Crystallogr.* **32**, 115–119 (1999).
25. Sheldrick, G. M. A short history of *SHELX*. *Acta Crystallogr. Sect. A* **64**, 112122 (2008).
26. Chakoumakos, B. C. et al. Four-circle single-crystal neutron diffractometer at the High Flux Isotope reactor. *J. Appl. Crystallogr.* **44**, 655–658 (2011).
27. Farrugia, L. J. Wingx and ortep for windows: An update. *J. Appl. Crystallogr.* **45**, 849–854 (2012).

28. Wills, A. A new protocol for the determination of magnetic structures using simulated annealing and representational analysis (SARAh). *Phys. B* **276**–**278**, 680–681 (2000).
29. Perez-Mato, J. M. et al. Symmetry-based computational tools for magnetic crystallography. *Annu. Rev. Mater. Res.* **45**, 217–248 (2015).
30. Rodrguez-Carvajal, J. Recent advances in magnetic structure determination by neutron powder diffraction. *Physica B* **192**, 55–69 (1993).
31. Zhang, A. et al. Interplay of Dirac electrons and magnetism in $CaMnB_2$ and $SrMnB_2$. *Nat. Commun.* **7**, 13833 (2016).
32. Zhu, F. et al. Magnetic structures, spin-flop transition, and coupling of Eu and Mn magnetism in the Dirac semimetal $EuMnBi_2$. *Phys. Rev. Res.* **2**, 043100 (2020).
33. Johnston, D. C. et al. Magnetic exchange interactions in $BaMn_2As_2$: A case study of the *J*1–*J*2–*Jc* Heisenberg model. *Phys. Rev. B* **84**, 094445 (2011).
34. Herrero-Martin, J. et al. Magnetic structure of $EuFe_2As_2$ as determined by resonant X-ray scattering. *Phys. Rev. B* **80**, 134411 (2009).
35. Xiao, Y. et al. Magnetic structure of $EuFe_2As_2$ determined by single-crystal neutron diffraction. *Phys. Rev. B* **80**, 174424 (2009).